nature metabolism

Brief Communication

https://doi.org/10.1038/s42255-025-01244-7

Reversible reduction in brain myelin content upon marathon running

Received: 18 March 2024

Accepted: 12 February 2025

Published online: 24 March 2025

Check for updates

Pedro Ramos-Cabrer[1,2,9], Alberto Cabrera-Zubizarreta[3,4,9], Daniel Padro[1], Mario Matute-González[5], Alfredo Rodríguez-Antigüedad[6,7,8] & Carlos Matute[7,8]

Here we use magnetic resonance imaging to study the impact of marathon running on brain structure in humans. We show that the signal for myelin water fraction—a surrogate of myelin content—is substantially reduced upon marathon running in specific brain regions involved in motor coordination and sensory and emotional integration, but recovers within two months. These findings suggest that brain myelin content is temporarily and reversibly diminished by severe exercise, a finding consistent with recent evidence from rodent studies that suggest that myelin lipids may act as glial energy reserves in extreme metabolic conditions.

Prolonged endurance exercise mobilizes energy stores throughout the body to meet energy demands. Marathon runners primarily rely on carbohydrates as the main energy source during a race[1]. Once glycogen becomes low in muscle, liver and other organs, including brain, marathon runners utilize fat as an energy source[1–4]. Fat is more abundant in the body than carbohydrates, and it can provide a sustained source of energy for prolonged endurance exercise.

Myelin surrounds and enwraps axons in the central and peripheral nervous systems, providing electrical insulation and metabolic support to axons. The primary components of myelin are lipids, which make up 70–80% of myelin, whereas myelin proteins compact and stabilize its multilayered structure. While oligodendroglial fatty acid metabolism has been proposed to serve as energy reserves during glucose deprivation[5], we further hypothesize that myelin lipids may contribute to brain activity as does body fat to fuel muscle.

To test our hypothesis we evaluated brain myelin content by multicomponent relaxometry magnetic resonance imaging (MRI) in city and mountain marathon runners. To that end, we acquired multi-echo T2-weighted MRI sequences post-processed with the DECAES algorithm for multicomponent relaxometry analysis[6], thus providing three-dimensional (3D) parametric maps of the myelin water fraction (MWF), a non-invasive surrogate imaging biomarker of myelin[6–8]. MWF measures pools of water molecules within myelin lamellae as a proxy, faithfully reflecting histological staining for myelin, and has high sensitivity to detect subtle variations in the myelin content[9]. In this manner, we estimated water trapped between the lipid bilayers of the myelin sheath around axons and excluded luminal water that accounts for intra- and extracellular water.

MRI-based MWF maps were constructed from $n = 10$ subjects within 48 h before running a marathon (Extended Data Fig. 1). All individuals showed a similar distribution of MWF across the brain, with naturally occurring, slight, interindividual variabilities. Maps of the luminal water fraction (LWF), myelin fraction T2 relaxation times and luminal fraction T2 relaxation times were also obtained in the fitting process. High-resolution 3D T1-weighted MRI images of all subjects showed no significant interindividual variability for the different imaging sessions (Extended Data Fig. 2). The absence of large differences among subjects allowed us to build up averaged MWF maps of the brain ($n = 10$; value ranges between 0 and 0.25). These value ranges are in line with MWF values found in healthy subjects over a wide range of ages (Extended Data Fig. 3)[10,11].

Similarly, averaged maps of MWF values were constructed for the second ($n = 10$ individuals), third ($n = 2$ individuals) and fourth ($n = 6$ individuals) imaging sessions, corresponding to post-run (24–48 h after the marathon), two weeks and two months (recovery) after the marathon, respectively. Coronal sections integrating imaging maps

[1]Center for Cooperative Research in Biomaterials (CIC biomaGUNE), Basque Research and Technology Alliance (BRTA), Donostia-San Sebastián, Spain. [2]Ikerbasque, Basque Foundation for Science, Bilbao, Spain. [3]Neuroradiology Department, MRI Unit, HT Médica, Jaén, Spain. [4]Osatek Magnetic Resonance Imaging Unit, Galdakao Hospital, Galdakao, Spain. [5]Radiology Department, Hospital Clinic Barcelona, Barcelona, Spain. [6]Department of Neurology, Cruces University Hospital, University of the Basque Country (UPV/EHU), Barakaldo, Spain. [7]Department of Neurosciences, University of the Basque Country (UPV/EHU) and CIBERNED-Instituto Carlos III, Leioa, Spain. [8]Biobizkaia Health Research Institute, Barkaldo, Spain. [9]These authors contributed equally: Pedro Ramos-Cabrer, Alberto Cabrera-Zubizarreta. e-mail: carlos.matute@ehu.eus

https://doi.org/10.1038/s42255-025-01244-7

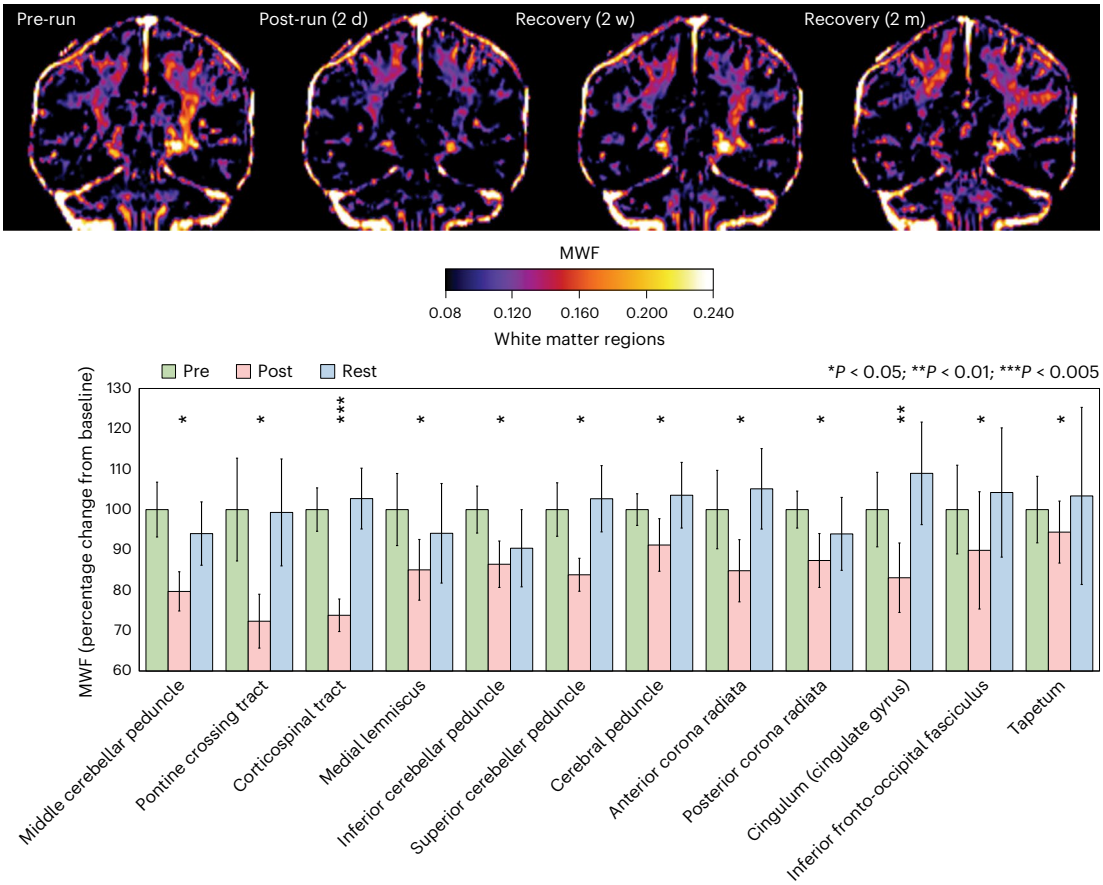

Fig. 1 | Myelin water fraction changes in white matter regions after running a marathon. Top, slab volumes (average intensity projection) of MWF maps from five consecutive coronal slices centred in motor descending pathways from an individual before the marathon (pre-run), two days after the marathon (post-run, 2 d) and two weeks after the marathon (post-run, 2 w), as well as after two months (2 m) of recovery. Bottom, histogram with mean ± s.e.m. values from all subjects ($n = 10$ for pre- and post-run, $n = 6$ for recovery) showing significant MWF reduction in white and grey matter areas 1–2 days after the marathon, and subsequent recovery to pre-run levels during two months of recovery. Individual data points for each histogram bar ($n = 20$ for pre- and post-run, $n = 12$ for recovery) originated from the two hemispheres in each subject. Notice that values return to pre-run levels in all areas. $^{*}P < 0.05$ and $^{***}P < 0.005$, one-tailed paired Student's t-test. See Extended Data Fig. 4 for exact P values and its Source Data for individual data points.

from a representative individual show a clear post-run reduction in MWF in motor descending pathways (Fig. 1, top).

Next, to obtain a comprehensive view of MWF changes, we analysed its values after segmentation of the entire brain into different regions with the help of an atlas-aided 3D morphometric analysis. Thus, we divided the brain into 50 white matter regions using the JHU brain atlas of white matter tracks[12] and 56 grey matter regions using the LPBA40 collection of the SRI24 brain atlas[13]. Mean MWF values were recorded for these 106 brain regions for each subject at each imaging session (https://doi.org/10.5281/zenodo.14726926 (ref. 14) and Fig. 2).

We focused on the regions with higher MWF values, as variations in this parameter are reflected better in more densely myelinated regions[15]. We observed consistent and significant region-variable MWF reductions in 12 white matter areas (Fig. 1, bottom, and Extended Data Fig. 4). In addition, MWF was lower in a few grey matter regions (Extended Data Fig. 4). However, lower myelin content in grey matter limits resolution to monitor MWF and those changes are uncertain.

MWF can be regarded as a strong correlate of myelin content reduction[15–18]; nevertheless, the exact correlation factor is to be determined, and, therefore, MWF-based studies should be considered as a semiquantitative evaluation of myelin content (see ref. 15 for a comprehensive analysis of MWF as a myelin imaging biomarker). An estimate of MWF changes versus ex vivo histopathological myelin quantification suggests that the former are typically larger than the latter[17], indicating that the reduction in myelin after marathon running should indeed be lower (approximately 40–50%) than the measured decrease in MWF.

Bilateral MWF loss in white matter was extensive after completion of the marathon, and its extent was similar in both hemispheres (Fig. 2). MWF was lower in the corticospinal tract, pontine crossing tract, cerebral and all three cerebellar peduncles, as well in the anterior and posterior corona radiata (for a complete list see Extended Data Fig. 4). Quantification of the changes illustrates that the MWF signal decreases significantly by up to 28% and 26% in the pontine crossing and corticospinal tracts, respectively (Figs. 1 and 2 and Extended Data Fig. 4). Thus, MWF robustly diminished in axonal tracts involving motor function and coordination along with sensory and emotional integration[19,20].

As MWF represents water trapped between myelin lamellae, a confounding factor of these changes could be dehydration. However, global dehydration would not change MWF by definition (for details see Extended Data Fig. 1). To rule out partial, regional dehydration, we measured total and partial central nervous system volumes. We found that the total brain, cerebrospinal fluid (CSF) (ventricles), grey matter, white matter, deep brain, brainstem and cerebellum volumes did not significantly change intra-individually across imaging sessions. Thus, P values for comparisons of paired brain regions post-run versus pre-run scans indicate, in all instances, absences of significant differences in the volume of all compared structures (Extended Data Fig. 5). These data are in line with previous studies showing that extensive

https://doi.org/10.1038/s42255-025-01244-7

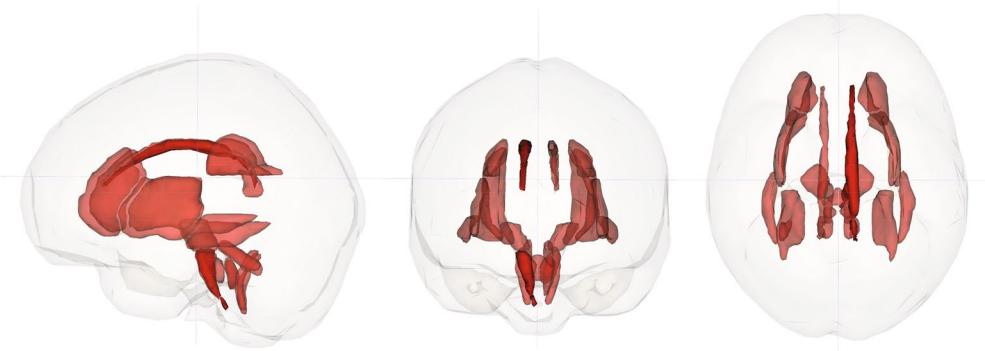

Fig. 2 | Colour-encoded representations of MWF changes in 3D. White matter areas that show a significant reduction in the MWF post-run ($n = 10$). Segmented white matter regions are displayed using the JHU atlas (https://neurovault.org/collections/264/ collection:264).

exercise does not alter brain volumes independently of the hydration state, as measured by MRI[21].

These observations are also consistent with previous findings showing that the level of hydration does not change MWF levels[22]. In turn, brain water volumes remain unaltered after extensive exercise[21]. Furthermore, MWF loss was not observed along the entire brain volume, as it would be as a consequence of dehydration, remaining unaltered in some axonal tracts (for example, corpus callosum), as well as in nearly all grey matter areas. Yet, and to exclude the possibility of selective dehydration in heavily myelinated territories, we calculated regional water content levels throughout the entire brain utilizing the grey and white matter atlases used to analyse MWFs. We found no significant differences in water content between pre- and post-run values in those areas showing significant reduction in MWF (Extended Data Figs. 6–8).

Collectively, these data provide solid evidence of bilateral MWF decrease after marathon running in motor- and non-motor-related brain connections, with a similar amplitude in each hemisphere. Notwithstanding, it is important to emphasize that the overall MWF reduction in the whole brain is limited and occurs in restricted areas, thus leaving the bulk of myelin unaffected.

We next examined whether MWF levels recover at rest after completion of the endurance effort. To that end, we performed MRI scans on runners ($n = 2$) two weeks after the run and found that, although there was a substantial partial increase of MWF values they did not reach pre-run levels (Fig. 1). These findings prompted us to measure MWF maps at later stages. We found that MWF values fully recovered from completion of the marathon two months after the run in all areas with MWF reduction (Fig. 1 and Extended Data Figs. 4 and 9; https://doi.org/10.5281/zenodo.14726926 (ref. 14). Thus, MWF status goes back to normal in myelinated tracts involved in motor and non-motor functions after two months of strenuous exercise.

Together, these findings provide compelling evidence that white matter tracts undergo a reduction in MWF that is later restored after recovery from prolonged endurance exercise. It would therefore be important to evaluate whether these changes transiently affect neurophysiological and cognitive functions associated with those regions.

Our findings show that running a marathon reduces runners' MWF levels in white matter areas, with a similar impact in both hemispheres. MWF values recover thereafter and reach pre-run values two months after the event. This reversible reduction in MWF upon prolonged exercise and recovery after lowering physical activity strongly suggests changes in myelin structure and content that may open up a new view of myelin as an energy store ready to use when common brain nutrients are in short supply. We define this process as metabolic myelin plasticity.

To assess myelin content we used MWF, an MRI imaging surrogate of myelin that faithfully represents its levels with a near linear relationship with ex vivo histopathological myelin quantification[15–18]. Accordingly, MWF values correlate with changes in myelin content, although they represent semiquantitative measurements of myelin. This limits an accurate account of the actual extent of myelin content changes. In turn, measured MWF may vary for reasons other than changes in myelin content, including increases in permeability of myelin membranes, alterations in iron concentration or axonal swelling. However, the impact of these features on MWF reduction in marathon runners is unlikely (see 'MWF confounding factors' and references therein).

Hitherto, changes in MWF have not been evaluated following strenuous, prolonged exercise. However, ultramarathon multistage runners may experience subtle reversible brain structural changes without neurological complications[23–28] along with increasing activity[29] because of energy deficits. This might result in usage of myelin-derived fatty acids for energy production. This idea is plausible, as glial cells can fuel neural metabolism by β-oxidation, and myelin peroxisomes are essential for white matter maintenance in flies and mice[5,30–32]. Thus, oligodendrocytes may survive glucose deprivation by local utilization of myelin lipids, which in turn allows oligodendrocytes to share energy substrates with axons to support their function[5]. Indeed, myelin-derived fatty acids can be β-oxidized and transferred into mitochondria for ATP production by CPT1A transport[5,33,34]. The amphipathic nature of these fatty acids makes them easily transferable to axons as well as to the surrounding glia and neurons and to support energy demands at various subcellular compartments. Thus, myelin turnover under low glucose conditions can transiently support axonal energy metabolism, a feature that may explain the gradual loss of myelin in neurodegenerative diseases with underlying hypometabolism[35].

Oligodendrocytes are particularly resistant to glucose withdrawal[36,37], and therefore use alternative mitochondria-dependent energy sources that may be relevant in pathology. Thus, continuous myelin turnover and fatty acid metabolism can help myelinated nerves to overcome a transient loss of glucose supply, thereby providing an energy reserve[5]. Indeed, ongoing inflammatory activity in multiple sclerosis lesions may compromise the energy support for (re)myelinating cells, while neuropathological findings in this demyelinating disease probably reflect defective oligodendroglial energy homeostasis[38].

Rather limited reduction in MWF, and presumably myelin, after completion of the marathon makes it unlikely that consumed myelin contributes to whole-body energy balance. However, we cannot rule out the possibility that it does in even more extreme exercise conditions and/or disease states, where nutrition is at stake (for example, anorexia nervosa and famine). Indeed, animal and human studies show that undernutrition negatively influences myelination[39–42]. In particular, dietary scarcity in anorexia nervosa leads to disturbances in cognition[43], paralleled with altered grey and white matter myelin and connectivity[44–49].

Regular, moderate-intensity, physical activity is a key factor in maintaining brain health across the lifespan[50]. By contrast, strenuous physical activity is a risk factor for amyotrophic lateral sclerosis (ALS) in individuals with a genetic predisposition to the disease[51,52]. Therefore, endurance exercise may pose an additional danger to heavily myelinated disease-vulnerable motor areas (for example, corticospinal tract) in individuals with ALS genetic risk, as myelin itself and myelin-producing oligodendrocytes are also vulnerable to glutamate excitotoxicity[53].

Myelin plasticity is fundamental to brain adaptation to neuronal activity, as it modifies myelin structure by increasing or decreasing the thickness of the myelin sheath[54,55]. Our findings strongly suggest that widespread reversible MWF reduction in endurance physical exercise represents a new form of plasticity to support brain function at the expense of myelin lipid use.

This pilot observational imaging study has limitations, including a relatively small number of participants that will require validation in a larger cohort, difficulty in assessing grey matter MWF changes due to relatively low myelin content that compromises the signal-to-noise ratio and limited spatial resolution due to long scanning times and the inherent slight movement of subjects. Nonetheless, the potential relevance of the findings described here to brain energy metabolism warrant additional studies.

Methods

Subjects

Runners were recruited at the Donostia city marathon 2022 ($n = 2$) and 2023 ($n = 2$), the Zegama-Aizkorri mountain marathon 2023 ($n = 2$), Hiru Handiak mountain marathon 2023 ($n = 2$) and Valencia city marathon ($n = 2$). No financial compensation was given to volunteers. All of them were well-trained men ($n = 8$) and woman ($n = 2$) aged 45–73-years-old who completed the trial in a healthy state. All subjects provided written informed consent before participation, including consent to share the information provided in the study, and the experiments were conducted in accordance with the Helsinki Declaration (2001). The procedure was approved by Comité de Etica de Investigación de Euskadi. Imaging sessions were carried out 24–48 hours before and after the marathon ($n = 10$), two weeks ($n = 2$) and two months later ($n = 6$) (Extended Data Fig. 10). Randomization was not necessary as we studied a single group of subjects. In all instances, individuals were well hydrated.

Data acquisition

MRI scans were acquired on a 3T whole-body MRI system (Achieva Dstream, Philips Medical System) using the internal quadrature body coil for transmission and a 32-channel phased array coil for reception. Each subject underwent an imaging protocol that included: (1) a multi-echo 3D gradient and spin–echo sequence (GRASE) for myelin water imaging, with the following parameters: TR = 2,000 ms; 32 echoes with a minimum echo time of 9.3 ms and maximum of 298 ms; SENSE 2.5; flip angle 90°, bandwidth in EPI frequency direction 2,591; field of view (FOV) 230 mm^2; 78 slices in transverse orientation; voxel size 1.2 × 1.2 × 1.8 mm^3; total scan time 7:08 min; and (2) a high-resolution T1w anatomical image in a sagittal orientation with the following parameters: TR = 7.4 ms; TE = 3.4 ms; matrix size 228 × 228; flip angle 9°; FOV 250 × 250 × 180 mm; slice thickness 1.1 m; 300 slices; acquisition time 4:55 min.

Image processing

Image processing and data analysis were performed blinded to group allocation during data collection. Raw data were exported in DICOM format for offline processing. First, data were converted into NIFTI format using dcm2niix[56]. Anatomical brain images (skull stripped out) were obtained from T1-weighted images applying BET[57] implementation from the FSL v.6.0 distribution[58]. Population distributions of T2 values were computed voxelwise from multi-echo data using Julia implementation DECAES software[6]. For the analysis of interindividual and intra-individual changes in MWF maps, all MWF maps for subjects at different imaging sessions (pre-run, post-run and recovery) were registered to a T2-weighted anatomical image of the brain of subject 1 (echo 8 of the echo train, with TE = 74.48 ms) at session 1 using ANT Syn registration[59]. For image segmentation and assessment of MWF values in different regions of the brain, T1-weighted images were nonlinearly registered to the JHU DTI-based white matter atlas for white matter track segmentation[12] and in parallel to the LPBA40 collection of the SRI24 brain atlas[13] for segmentation of grey matter regions. Transformation matrices were later applied to the MWF maps, previously linearly registered to the corresponding T1W image. Further image processing for the creation of figures was performed with the freely available software FIJI (ImageJ v.2.0) and ITK-Snap v.4.0.1. Individual MWF data are provided in https://doi.org/10.5281/zenodo.14726926 (ref. 14).

Statistics

We used Microsoft Excel (Office 365, 2024 version) for statistical analyses, and values were calculated as mean ± standard deviation of the mean (s.d.) or standard error of the mean (s.e.m.). Statistical significance was defined as $^*P < 0.05$, $^{**}P < 0.01$, $^{***}P < 0.005$ (or as otherwise indicated in figure captions). No statistical methods were used to predetermine sample sizes but our sample sizes are similar to those reported in previous publications[60]. Data distribution was assumed to be normal but this was not formally tested. Post-run versus pre-run groups, or recovery versus post-run groups, were compared using a one-tailed paired Student's t-test. Each participant was analysed separately and measurements across imaging sessions normalized to pre-run data. We made all statistical analysis and compared subjects post versus pre ($n = 10$), and recovery versus pre (2 months, $n = 6$). For the comparison of the different brain regions, we used MWF mean values obtained for both left and right hemispheres. For the analysis of percentage of change in MWF values, pretreatment of the data was performed to eliminate outliers using the interquartile (IQR) method[61], discarding all data below Q1 − 1.5 × IQR or over Q3 + 1.5 × IQR limits.

Technical considerations and limitations

Multi-echo T2 sequences allow differentiation between water with different T2 relaxation times. Water in the brain is located in the CSF, extracellular space, intracellular space and between myelin layers. Approximately 70–85% of the brain mass is water, and approximately 40% of the mass in myelinated axonal tracts is compartmentalized water.

In human white matter, the MRI signal from water can be separated into three pools on the basis of the T2 relaxation time. The longest T2 component is due to CSF. The intermediate component arises from both intracellular and extracellular water (LWF), and the shortest T2 component is due to water trapped between myelin bilayers (or MWF). CSF is often neglected in myelin imaging with MRI because of the low amount of CSF in the white matter[62]. MWF is defined as the ratio of the area of short T2 components to the area of all T2 components[7,16]. The ranges of T2 relaxation time used for the assignment of MWF and LWF where 0–30 ms and 30–200 ms, respectively, in line with current standards[7]. This fully distinguished the myelin-bound and luminal populations.

T2 mapping is a well-established method for myelin quantification. Originally, a T2 multi-echo spin–echo sequence was developed, but the main drawback was the long scanning time, which prevented its application in clinical scenarios. In recent years, together with other methods, a combined GRASE sequence has been adopted for myelin water imaging (MWI), reducing the acquisition time to less than 10 min with full brain coverage[63]. Reproducibility of MWI with this technique

has been demonstrated in a multisite, multivendor study[64] and with different reconstruction methods[65].

However, MWI with T2 mapping is not without challenges, and several factors need to be considered. The signal-to-noise ratio in MWI with T2 mapping is low. The myelin signal decays rapidly as the MWF is approximately 10%, and the relaxation time of myelin water is relatively short at 10 ms, which makes changes in MWF difficult to detect[66].

MWF confounding factors. A possible confounding effect on assimilating MWF to myelin content is brain oedema, which may occur in strenuous exercise, such as high mountain ultramarathons, but has not been observed in 42.195-km marathons[25,67]. Moreover, oedema/inflammation during new lesion formation in multiple sclerosis has a minor impact, if any, on MWF[60]. These previous reports indicate that even if minor oedema appears in a standard marathon run, the impact on MWF would be marginal.

Another confounding factor can be iron, the main source of paramagnetic susceptibility in the brain[68]. Iron shortens T2 components and thus potentially increases MWF values[69]. Thus, total iron depletion in experimental animals reduces MWF values by one-fourth[69]. However, serum iron levels increase or remain similar after ultramarathon and marathon running, respectively[70,71]. Therefore, it is unlikely that changes in iron homeostasis contribute significantly to MWF reduction after prolonged endurance exercise, and, if so, it may underestimate real myelin content reduction.

Lastly, fibre orientation may also affect myelin water T2, as well as the intracellular and extracellular water T2; however, MWF has a weaker innate orientation dependence[9]. Moreover, MWF value comparisons within and among subjects at all stages were made at similar MRI plane levels and orientations.

Reporting summary

Further information on research design is available in the Nature Portfolio Reporting Summary linked to this article.

Data availability

Numerical data and materials used in this work are available via Zenodo at https://doi.org/10.5281/zenodo.14726926 (ref. 14). Images from subjects are available upon request (contact: Pedro Ramos-Cabrer, pramos@cicbiomagune.es). Source data are provided with this paper.

Code availability

Code used in this work is available via Zenodo at https://doi.org/10.5281/zenodo.14726926 (ref. 14).

References

1. Burke, L. M. & Hawley, J. A. Swifter, higher, stronger: what's on the menu? *Science* **362**, 781–787 (2018).
2. Alghannam, A. F., Ghaith, M. M. & Alhussain, M. H. Regulation of energy substrate metabolism in endurance exercise. *Int. J. Environ. Res. Public Health* **18**, 4963 (2021).
3. Matsui, T. et al. Astrocytic glycogen-derived lactate fuels the brain during exhaustive exercise to maintain endurance capacity. *Proc. Natl Acad. Sci. USA* **114**, 6358–6363 (2017).
4. Magistretti, P. J. & Allaman, I. Acellular perspective on brain energy metabolism and functional imaging. *Neuron* **86**, 883–901 (2015).
5. Asadollahi, E. et al. Oligodendroglial fatty acid metabolism as a central nervous system energy reserve. *Nat. Neurosci.* **27**, 1934–1944 (2024).
6. Doucette, J., Kames, C. & Rauscher, A. DECAES—decomposition and component analysis of exponential signals. *Z. Med. Phys.* **30**, 271–278 (2020).
7. MacKay, A. L. & Laule, C. Magnetic resonance of myelin water: an in vivo marker for myelin. *Brain Plast.* **2**, 71–91 (2016).
8. Caverzasi, E. et al. MWF of the corpus callosum is a robust measure of remyelination: results from the ReBUILD trial. *Proc. Natl Acad. Sci. USA* **120**, e2217635120 (2023).
9. Morris, S. R. et al. Myelin biomarkers in the healthy adult brain: correlation, reproducibility, and the effect of fiber orientation. *Magn. Reson. Med.* **89**, 1809–1824 (2023).
10. Dvorak, A. V. et al. An atlas for human brain myelin content throughout the adult life span. *Sci. Rep.* **11**, 269 (2021).
11. Kiely, M. et al. Insights into human cerebral white matter maturation and degeneration across the adult lifespan. *NeuroImage* **15**, 118727 (2022).
12. Mori, S., Wakana, S., van Zijl, P. C. M. & Nagae-Poetscher, L. M. *MRI Atlas of Human White Matter* (Elsevier, 2005).
13. Rohlfing, T., Zahr, N. M., Sullivan, E. V. & Pfefferbaum, A. The SRI24 multichannel atlas of normal adult human brain structure. *Hum. Brain Mapp.* **31**, 798–819 (2010).
14. Ramos-Cabrer, P. et al. Source data and code. *Zenodo* https://doi.org/10.5281/zenodo.14726926 (2025).
15. Laule, C. et al. Magnetic resonance imaging of myelin. *Neurotherapeutics* **4**, 460–484 (2007).
16. Mackay, A. et al. In vivo visualization of myelin water in brain by magnetic resonance. *Magn. Reson. Med.* **31**, 673–677 (1994).
17. Laule, C. et al. Myelin water imaging in multiple sclerosis: quantitative correlations with histopathology. *Mult. Scler.* **12**, 747–753 (2006).
18. Laule, C. et al. Myelin water imaging of multiple sclerosis at 7 T: correlations with histopathology. *NeuroImage* **40**, 1575–1580 (2008).
19. Bubb, E. J., Nelson, A. J. D., Cozens, T. C. & Aggleton, J. P. Organisation of cingulum bundle fibres connecting the anterior thalamic nuclei with the rodent anterior cingulate and retrosplenial cortices. *Brain Neurosci. Adv.* **4**, 2398212820957160 (2020).
20. Verhulst, M. M. L. H., Glimmerveen, A. B., van Heugten, C. M., Helmich, R. C. G. & Hofmeijer, J. MRI factors associated with cognitive functioning after acute onset brain injury: Systematic review and meta-analysis. *NeuroImage Clin.* **38**, 103415 (2023).
21. Dieleman, N., Koek, H. L. & Hendrikse, J. Short-term mechanisms influencing volumetric brain dynamics. *NeuroImage Clin.* **16**, 507–513 (2017).
22. Meyers, S. M. et al. Does hydration status affect MRI measures of brain volume or water content? *J. Magn. Reson. Imaging* **44**, 296–304 (2016).
23. Gliner, J. A., Matsen-Twisdale, J. A., Horvath, S. M. & Maron, M. B. Visual evoked potentials and signal detection following a marathon race. *Med. Sci. Sports* **11**, 155–159 (1979).
24. Freund, W. et al. Substantial and reversible brain gray matter reduction but no acute brain lesions in ultramarathon runners: experience from the TransEurope-FootRace Project. *BMC Med.* **10**, 170 (2012).
25. Herm, J. et al. MRI brain changes after marathon running: results of the Berlin Beat of Running study. *Int. J. Sports Med.* **40**, 856–862 (2019).
26. Ozdurak Singin, R. H., Duz, S. & Kiraz, M. Cortical and subcortical brain volume alterations following endurance running at 38.6 km and 119.2 km in male athletes. *Med. Sci. Monit.* **27**, e926060 (2021).
27. Bailey, S. P., Hall, E. E., Folger, S. E. & Miller, P. C. Changes in EEG during graded exercise on a recumbent cycle ergometer. *J. Sports Sci. Med.* **7**, 505–511 (2008).
28. Brümmer, V., Schneider, S., Strüder, H. K. & Askew, C. D. Primary motor cortex activity is elevated with incremental exercise intensity. *Neuroscience* **181**, 150–162 (2011).
29. Saab, A. S. et al. Oligodendroglial NMDA receptors regulate glucose import and axonal energy metabolism. *Neuron* **91**, 119–132 (2016).

30. Kassmann, C. M. Myelin peroxisomes – essential organelles for the maintenance of white matter in the nervous system. *Biochimie* **98**, 111–118 (2014).
31. McMullen, E. et al. Glycolytically impaired *Drosophila* glial cells fuel neural metabolism via β-oxidation. *Nat. Commun.* **14**, 2996 (2023).
32. Kassmann, C. M. et al. Axonal loss and neuroinflammation caused by peroxisome-deficient oligodendrocytes. *Nat. Genet.* **39**, 969–976 (2007).
33. Bolaños, J. P. Bioenergetics and redox adaptations of astrocytes to neuronal activity. *J. Neurochem.* **139**, 115–125 (2016).
34. Morant-Ferrando, B. et al. Fatty acid oxidation organizes mitochondrial supercomplexes to sustain astrocytic ROS and cognition. *Nat. Metab.* **5**, 1290–1302 (2023).
35. Zilberter, Y., Tabuena, D. R. & Zilberter, M. NOX-induced oxidative stress is a primary trigger of major neurodegenerative disorders. *Prog. Neurobiol.* **231**, 102539 (2023).
36. Narine, M. & Colognato, H. Current insights into oligodendrocyte metabolism and its power to sculpt the myelin landscape. *Front. Cell. Neurosci.* **16**, 892968 (2022). 28.
37. Fern, R., Davis, P., Waxman, S. G. & Ransom, B. R. Axon conduction and survival in CNS white matter during energy deprivation: a developmental study. *J Neurophysiol.* **N79N**, 95–105 (1998).
38. Tepavčević, V. Oligodendroglial energy metabolism and (re) myelination. *Life* **11**, 238 (2021).
39. Laczkovics, C. et al. White matter integrity is disrupted in adolescents with acute anorexia nervosa: a diffusion tensor imaging study. *Psychiatry Res. Neuroimaging* **320**, 111427 (2022).
40. Krigman, M. R. & Hogan, E. L. Undernutrition in the developing rat: effect upon myelination. *Brain Res.* **107**, 239–255 (1976).
41. Wiggins, R. C. & Fuller, G. N. Relative synthesis of myelin in different brain regions of postnatally undernourished rats. *Brain Res.* **162**, 103–112 (1979).
42. Connor, J. R. & Menzies, S. L. Relationship of iron to oligodendrocytes and myelination. *Glia* **17**, 83–93 (1996).
43. *Diagnostic and Statistical Manual of Mental Disorders (DSM-5)* (American Psychiatric Association, 2013).
44. Katzman, D. K. et al. Cerebral gray matter and white matter volume deficits in adolescent girls with anorexia nervosa. *J. Pediatr.* **129**, 794–803 (1996).
45. Boto, J. et al. Cerebral gray and white matter involvement in anorexia nervosa evaluated by T1, T2, and T2* mapping. *J. Neuroimaging* **29**, 598–604 (2019).
46. Gaudio, S., Carducci, F., Piervincenzi, C., Olivo, G. & Schiöth, H. B. Altered thalamo–cortical and occipital–parietal–temporal–frontal white matter connections in patients with anorexia and bulimia nervosa: a systematic review of diffusion tensor imaging studies. *J. Psych. Neurosci.* **44**, 324 (2019).
47. Lloyd, E. C. et al. Large-scale exploration of whole-brain structural connectivity in anorexia nervosa: alterations in the connectivity of frontal and subcortical networks. *Biol. Psychiatry Cogn. Neurosci. Neuroimaging* **8**, 864–873 (2023).
48. Pappaianni, E. et al. Initial evidence of abnormal brain plasticity in anorexia nervosa: an ultra-high field study. *Sci. Rep.* **12**, 2589 (2022).
49. Watson, H. J. et al. Genome-wide association study identifies eight risk loci and implicates metabo-psychiatric origins for anorexia nervosa. *Nat. Genet.* **51**, 1207–1214 (2019).
50. Kirkinezos, I. G., Hernandez, D., Bradley, W. G. & Moraes, C. T. Regular exercise is beneficial to a mouse model of amyotrophic lateral sclerosis. *Ann. Neurol.* **53**, 804–807 (2003).
51. Chapman, L., Cooper-Knock, J. & Shaw, P. J. Physical activity as an exogenous risk factor for amyotrophic lateral sclerosis: a review of the evidence. *Brain* **146**, 1745–1757 (2023).
52. Zheng, X. et al. Physical activity as risk factor in amyotrophic lateral sclerosis: a systematic review and meta-analysis. *J. Neurol.* **270**, 2438–2450 (2023).
53. Matute, C., Sánchez-Gómez, M. V., Martínez-Millán, L. & Miledi, R. Glutamate receptor-mediated toxicity in optic nerve oligodendrocytes. *Proc. Natl Acad. Sci. USA* **94**, 8830–8835 (1997).
54. Fields, R. D. & Dutta, D. J. Treadmilling model for plasticity of the myelin sheath. *Trends Neurosci.* **42**, 443–447 (2019).
55. Knowles, J. K., Batra, A., Xu, H. & Monje, M. Adaptive and maladaptive myelination in health and disease. *Nat. Rev. Neurol.* **18**, 735–746 (2022).
56. Li, X., Morgan, P. S., Ashburner, J., Smith, J. & Rorden, C. The first step for neuroimaging data analysis: DICOM to NIfTI conversion. *J. Neurosci. Methods* **264**, 47–56 (2016).
57. Smith, S. M. Fast robust automated brain extraction. *Hum. Brain Mapp.* **17**, 143–155 (2002).
58. Jenkinson, M., Beckmann, C. F., Behrens, T. E., Woolrich, M. W. & Smith, S. M. FSL. *NeuroImage* **62**, 782–790 (2012).
59. Avants, B. B., Epstein, C. L., Grossman, M. & Gee, J. C. Symmetric diffeomorphic image registration with cross-correlation: evaluating automated labeling of elderly and neurodegenerative brain. *Med. Image Anal.* **12**, 26–41 (2008).
60. Vavasour, I. M. et al. Water content changes in new multiple sclerosis lesions have a minimal effect on the determination of myelin water fraction values. *J. Neuroimaging* **31**, 1119–1125 (2021).
61. Smiti, A. A critical overview of outlier detection methods. *Comp. Sci. Rev.* **38**, 100306 (2020).
62. Henkelman, R. M., Stanisz, G. J. & Graham, S. J. Magnetization transfer in MRI: a review. *NMR Biomed.* **14**, 57–64 (2001).
63. Prasloski, T. et al. Rapid whole cerebrum myelin water imaging using a 3D GRASE sequence. *NeuroImage* **63**, 533–599 (2012).
64. Lee, L. E. et al. Inter-vendor reproducibility of myelin water imaging using a 3D gradient and spin echo sequence. *Front. Neurosci.* **12**, 854 (2018).
65. Fischi-Gomez, E. et al. Variability and reproducibility of multi-echo T2 relaxometry: insights from multi-site, multi-session and multi-subject MRI acquisitions. *Front. Radiol.* **2**, 930666 (2022).
66. van der Weijden, C. W. J. et al. Quantitative myelin imaging with MRI and PET: an overview of techniques and their validation status. *Brain* **146**, 1243–1266 (2023).
67. Zanchi, D. et al. Extreme mountain ultra-marathon leads to acute but transient increase in cerebral water diffusivity and plasma biomarkers levels changes. *Front. Physiol.* **7**, 664 (2017).
68. Deistung, A., Schweser, F. & Reichenbach, J. R. Overview of quantitative susceptibility mapping. *NMR Biomed.* **30**, e3569 (2017).
69. Birkl, C. et al. The influence of brain iron on myelin water imaging. *NeuroImage* **199**, 545–552 (2019).
70. Kaufmann, C. C. et al. Effect of marathon and ultra-marathon on inflammation and iron homeostasis. *Scand. J. Med. Sci. Sports* **31**, 542–552 (2021).
71. Kłapcińska, B. et al. Metabolic responses to a 48-h ultra-marathon run in middle-aged male amateur runners. *Eur. J. Appl. Physiol.* **113**, 2781–2793 (2013).

Acknowledgements

We thank runner volunteers for their generosity and patience. A. Planas, J. J. Lucas, F. M. Goñi, F. Kirchhoff, G. Foffani, J. P. Bolaños, A. Volterra, M. M. Panicker and F. Pérez-Cerdá for insightful discussions and suggestions on the manuscript. We also thank Osatek-Galdakao for providing human imaging facilities for MRI scans. Funding: Spanish Ministry of Science and Innovation and Universities grants PID2022-143020OB-I00 (C.M.), PID2023-152005OB-I00 (P.R.-C.), Basque Government grant IT-1551-22 (C.M.) Basque Government

grant KK-2021/0009 (P.R.-C.). CIBERNED Network, Instituto Carlos III, grant CB06/05/0076 (C.M.), Ikerbasque Foundation, the Ikerbasque Research Professors Program (P.R.-C.).

Author contributions

Conceptualization: P.R.-C., C.M. Methodology: P.R.-C., A.C.-Z., D.P., M.M.-G., A.R.-A., C.M. Investigation: P.R.-C., A.C.-Z., D.P., M.M.-G., A.R.-A., C.M. Funding acquisition: P.R.-C., C.M. Supervision: P.R.-C., C.M. Writing—original draft: P.R.-C., C.M. Writing—review and editing: P.R.-C., A.C.-Z., D.P., M.M.-G., A.R.-A., C.M.

Competing interests

The authors declare no competing interests.

Additional information

Extended data is available for this paper at https://doi.org/10.1038/s42255-025-01244-7.

Supplementary information The online version contains supplementary material available at https://doi.org/10.1038/s42255-025-01244-7.

Correspondence and requests for materials should be addressed to Carlos Matute.

Peer review information *Nature Metabolism* thanks Alex MacKay and the other, anonymous, reviewer(s) for their contribution to the peer review of this work. Primary Handling Editor: Alfredo Giménez-Cassina, in collaboration with the *Nature Metabolism* team.

https://doi.org/10.1038/s42255-025-01244-7

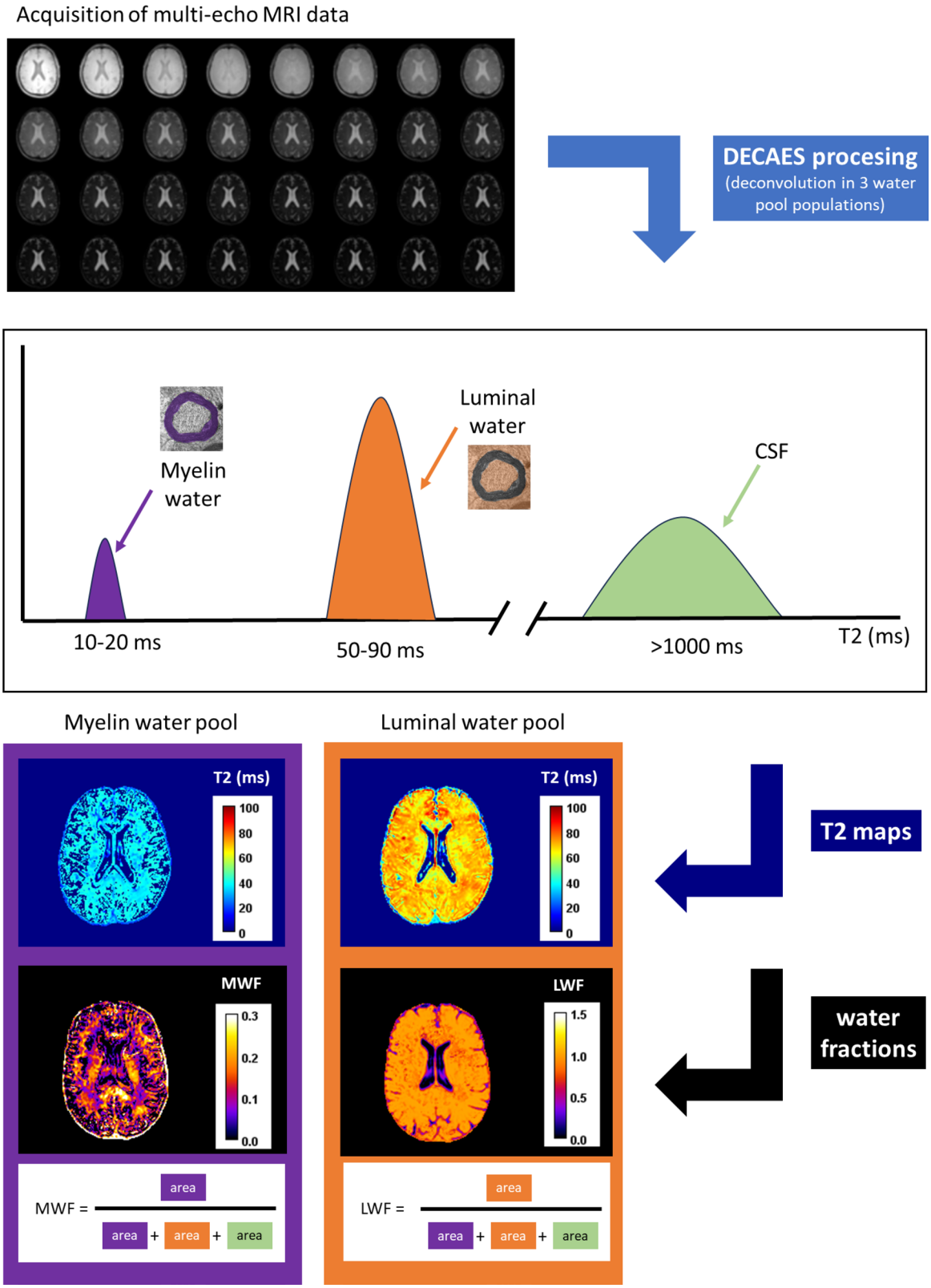

Extended Data Fig. 1 | Schematic representation of the DECAES procedure to extract myelin water fraction (MWF) values. MRI T2 weighted multi-echo images were processed using decomposition and component analysis of exponential signals (DECAES). This procedure uses the relaxation curves in each pixel to deconvolve the signal from 3 different pools of water: 1) water protons in myelin sheaths (short T2 values), 2) inter- and intracellular water molecules (luminal water fraction, with intermediate T2 values), and 3) signal from CSF (unrestricted water pool, with very large T2 values). Thus, a set of two T2 maps (short T2 population and intermediate T2 population, the CSF contribution is generally obviated) are generated, along with two maps of water fraction (% of contribution of that fraction to the total signal), one reflecting MWF and the other reflecting the luminal water fraction (LWF). The approach used in this study computes MWF derived from the area of myelin protons without differentiating luminal protons and unrestricted water pools whose combined area is estimated, as established by Doucette et al.[6], MacKay et al.[7], Caverzasi et al.[8] ms, millisecond.

https://doi.org/10.1038/s42255-025-01244-7

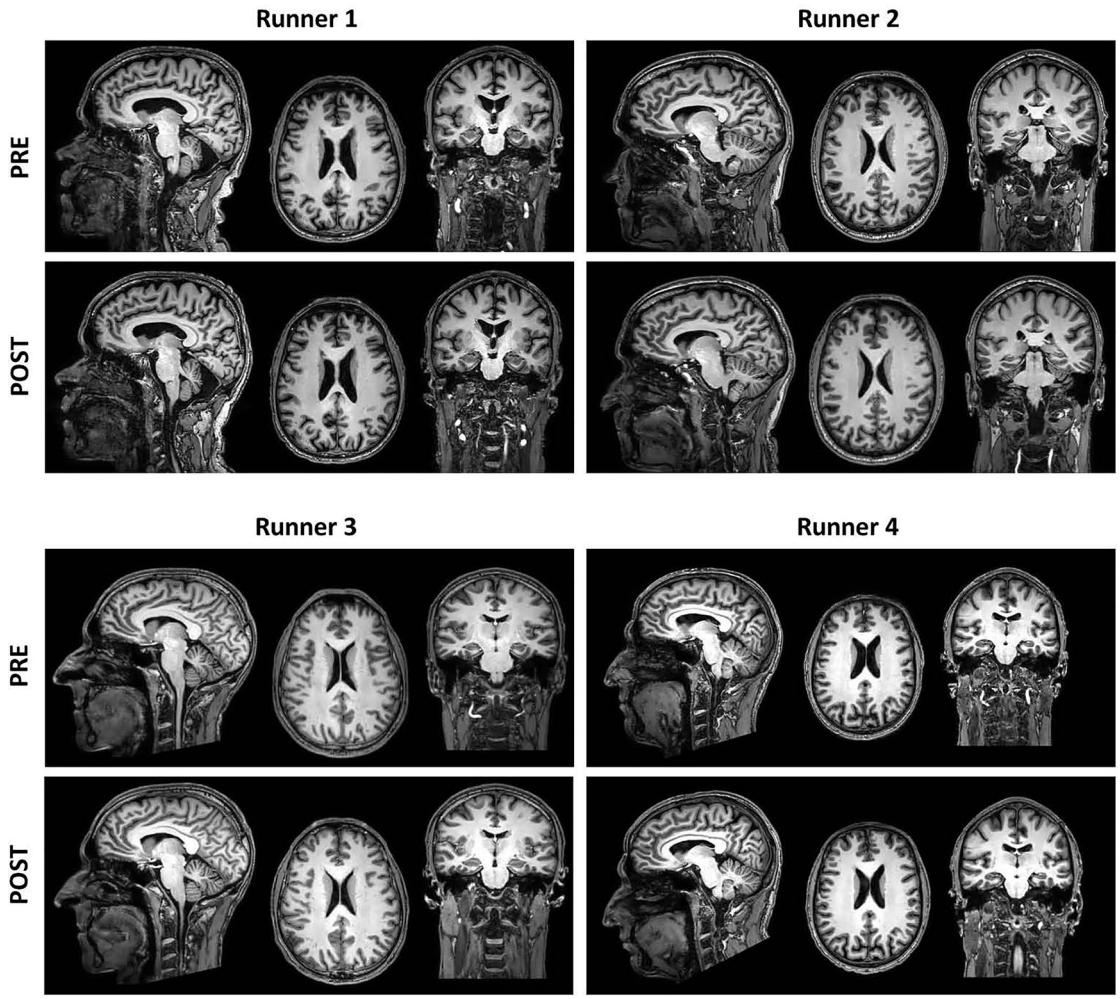

Extended Data Fig. 2 | High-resolution 3D T1-weighted MRI images of four representative subjects. Sagittal, axial and coronal views of the 3D images acquired with T1 weighting for anatomical reference, pre- and post-run. Images show no significant interindividual differences for the different imaging sessions. Volumes of whole brain and structures was unaltered (see also Extended Data Fig. 5).

https://doi.org/10.1038/s42255-025-01244-7

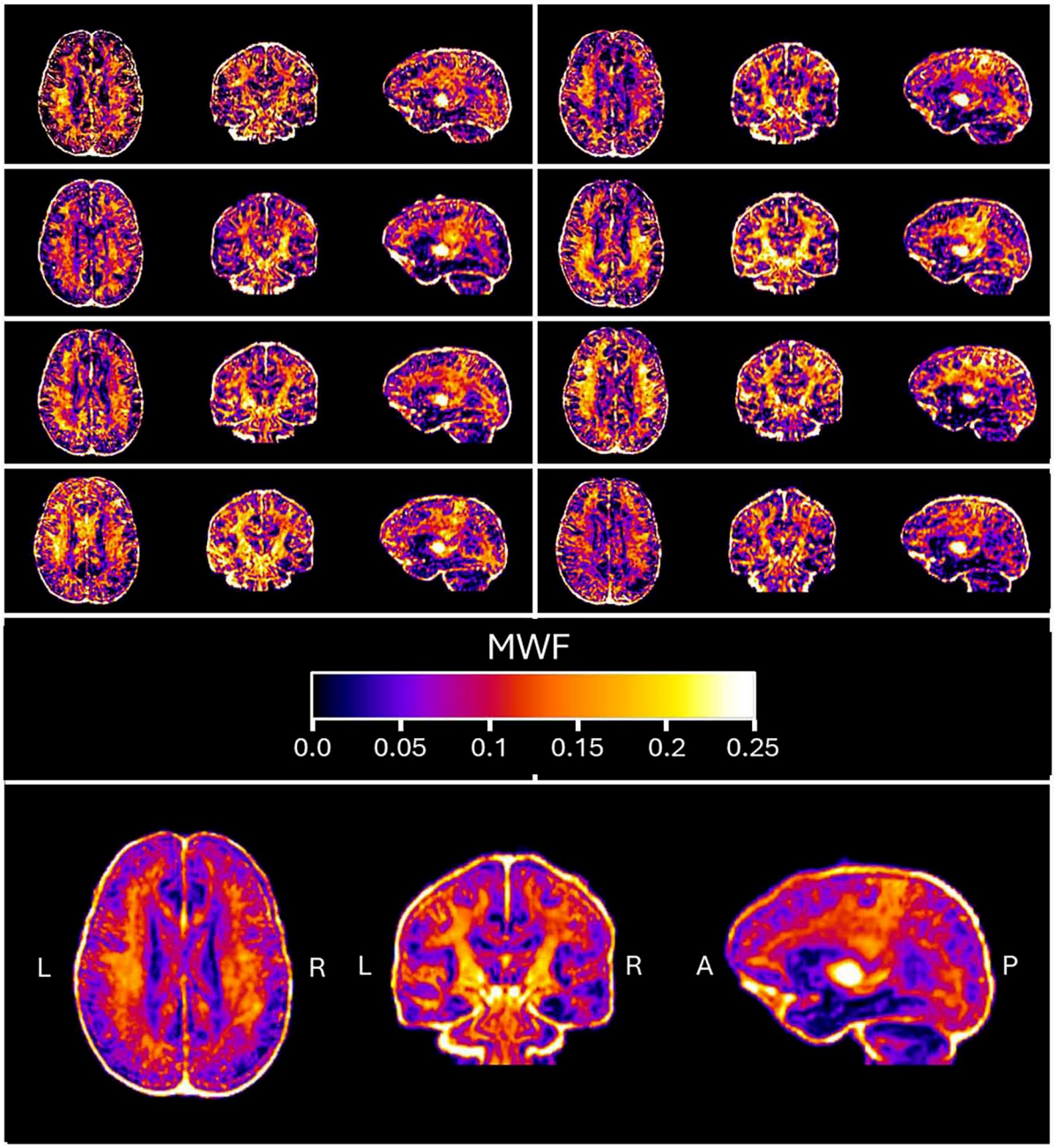

Extended Data Fig. 3 | Myelin water fraction (MWF) parametric maps from representative subjects before the marathon challenge. Top) Pre-exercise MWF maps for subjects scanned in this study. From top to bottom, arbitrarily chosen axial, coronal and sagittal planes. Bottom) Average maps obtained after ANTs Syn registration of all images to a common spatial frame.

https://doi.org/10.1038/s42255-025-01244-7

Region	Mean (% pre-run)			SEM			Student's t values	
White Matter	Pre-run	Post-run	Recovery (2 mo)	Pre-run	Post-run	Recovery (2 mo)	Post vs Pre	Recov. vs Pre
Middle cerebellar peduncle	100	80	94	6,8	4,9	5,6	0,018	0,214
Pontine crossing tract	100	72	99	12,7	6,7	12,3	0,031	0,288
Genu of corpus callosum	100	84	109	6,5	10,2	11,5	0,099	0,217
Body of corpus callosum	100	103	117	1,7	9,1	10,3	0,151	0,250
Splenium of corpus callosum	100	93	97	7,5	6,9	13,2	0,220	0,472
Fornix (column and body)	100	85	105	10,1	16,2	21,3	0,296	0,429
Corticospinal tract	100	74	103	5,4	4,0	7,2	0,000	0,475
Medial lemniscus	100	85	94	8,9	7,5	11,9	0,037	0,117
Inferior cerebellar peduncle	100	86	90	5,8	5,8	9,2	0,039	0,052
Superior cerebellar peduncle	100	84	103	6,6	4,1	7,9	0,015	0,493
Cerebral peduncle	100	87	104	3,9	5,2	7,8	0,013	0,349
Anterior limb of internal capsule	100	84	104	10,0	9,0	14,6	0,175	0,458
Posterior limb of internal capsule	100	91	105	5,4	7,3	7,5	0,076	0,470
Retrolenticular part of internal capsule	100	92	107	6,7	6,5	11,7	0,069	0,346
Anterior coronaadiata	100	85	105	9,7	7,7	9,6	0,017	0,495
Superior coronaadiata	100	99	115	7,8	6,3	9,1	0,436	0,074
Posterior coronaadiata	100	87	94	4,6	6,7	8,7	0,026	0,455
Posterior thalamicadiation	100	103	101	6,5	5,5	13,0	0,243	0,451
Sagittal stratum	100	103	103	6,5	6,6	11,4	0,358	0,494
External capsule	100	89	111	8,8	9,4	13,6	0,056	0,369
Cingulum (cingulate gyrus)	100	83	109	9,2	8,6	12,2	0,003	0,295
Cingulum (hippocampus)	100	83	112	11,0	10,7	15,4	0,085	0,258
Fornix (cres) / Stria terminalis	100	93	117	10,9	7,8	14,6	0,246	0,217
Superior longitudinal fasciculus	100	102	116	7,2	7,2	9,5	0,320	0,029
Superior fronto-occipital fasciculus	100	84	112	10,5	9,0	14,1	0,171	0,352
Inferior fronto-occipital fasciculus	100	80	103	9,6	9,0	13,6	0,011	0,417
Uncinate fasciculus	100	91	99	14,2	9,0	19,6	0,081	0,347
Tapetum	100	86	91	8,2	5,2	19,0	0,048	0,442
Gray Matter								
superior frontagyrus	100	100	98	5,0	5,8	4,6	0,389	0,452
middle frontagyrus	100	101	100	9,3	9,3	8,6	0,367	0,380
inferior frontagyrus	100	84	98	8,2	6,9	8,0	0,016	0,313
precentragyrus	100	110	107	6,0	6,8	5,9	0,028	0,246
middle orbitofrontagyrus	100	94	101	7,7	7,1	5,7	0,094	0,275
lateraorbitofrontagyrus	100	91	100	6,4	7,3	5,0	0,075	0,464
gyrus rectus	100	110	85	8,9	9,8	10,5	0,167	0,018
postcentragyrus	100	107	106	5,6	7,6	4,5	0,089	0,107
superior parietagyrus	100	110	125	7,0	8,0	11,2	0,149	0,000
supramarginagyrus	100	104	90	10,8	10,9	11,7	0,450	0,175
angular gyrus	100	107	112	11,8	12,9	14,6	0,290	0,071
precuneus	100	93	108	6,9	8,9	12,3	0,251	0,131
superior occipitagyrus	100	114	126	8,0	7,0	5,9	0,035	0,001
middle occipitagyrus	100	111	112	6,7	8,4	9,0	0,147	0,082
inferior occipitagyrus	100	93	98	6,2	8,6	8,7	0,142	0,362
cuneus	100	105	107	6,5	5,9	6,4	0,253	0,114
superior temporagyrus	100	94	91	7,5	8,3	7,4	0,234	0,039
middle temporagyrus	100	85	77	6,9	6,8	7,3	0,002	0,004
inferior temporagyrus	100	93	91	6,8	8,4	7,7	0,165	0,023
parahippocampagyrus	100	87	106	6,0	5,1	8,7	0,009	0,249
linguagyrus	100	97	105	4,6	5,3	8,4	0,283	0,123
fusiform gyrus	100	101	111	8,9	9,5	12,8	0,292	0,321
insular cortex	100	75	99	4,6	6,9	11,7	0,003	0,443
cingulate gyrus	100	77	105	5,4	5,2	9,5	0,000	0,196
caudate	100	98	87	10,3	11,9	14,3	0,472	0,301
putamen	100	92	97	8,3	9,8	14,1	0,244	0,312
hippocampus	100	95	116	9,0	9,6	12,5	0,302	0,149
cerebellum	100	86	92	7,0	5,3	4,3	0,065	0,131
brainstem	100	79	102	5,8	5,6	8,0	0,024	0,360

Extended Data Fig. 4 | Myelin water fraction changes (%) in brain regions post-run and after 2 months of recovery. one-tail paired Student's t-test.

https://doi.org/10.1038/s42255-025-01244-7

Region	Pre-run										V (cm^3)			Post vs Pre
	S1	S2	S3	S4	S5	S6	S7	S8	S9	S10	Mean	SDV	SEM	Student's t values
Total brain tissue	1383	1222	1372	1379	1234	1357	1235	1331	1069	985	1257	138	44	0.196
CSF	290	223	235	232	242	254	241	252	188	189	235	30	10	0.445
Gray matter	610	559	621	623	560	628	583	626	507	448	576	60	19	0.155
White matter	483	440	516	524	433	475	411	453	374	348	446	57	18	0.249
Deep brain	47	47	49	48	41	48	41	45	39	37	44	4	1	0.232
brainstem	23	24	23	24	19	22	20	24	19	21	22	2	1	0.493
Cerebellum	138	155	147	148	132	137	141	164	138	131	143	10	3	0.192
Region	Post-run										V (cm^3)			
	S1	S2	S3	S4	S5	S6	S7	S8	S9	S10	Mean	SDV	SEM	
Total brain tissue	1385	1226	1379	1237	1234	1347	1239	1336	1071	984	1244	131	42	
CSF	291	220	232	239	240	254	244	251	187	189	235	31	10	
Gray matter	609	561	623	563	559	615	584	629	508	448	570	57	18	
White matter	485	445	524	435	435	478	411	456	376	347	439	52	16	
Deep brain	46	47	48	42	42	48	41	45	40	38	44	4	1	
brainstem	23	24	24	19	20	22	21	24	20	22	22	2	1	
Cerebellum	139	154	148	133	132	136	143	164	137	131	142	11	3	

Extended Data Fig. 5 | Volumes of brain regions across subjects and pre-run and post-run MRI sessions. Student's t values were calculated using a one-tail paired t-test.

https://doi.org/10.1038/s42255-025-01244-7

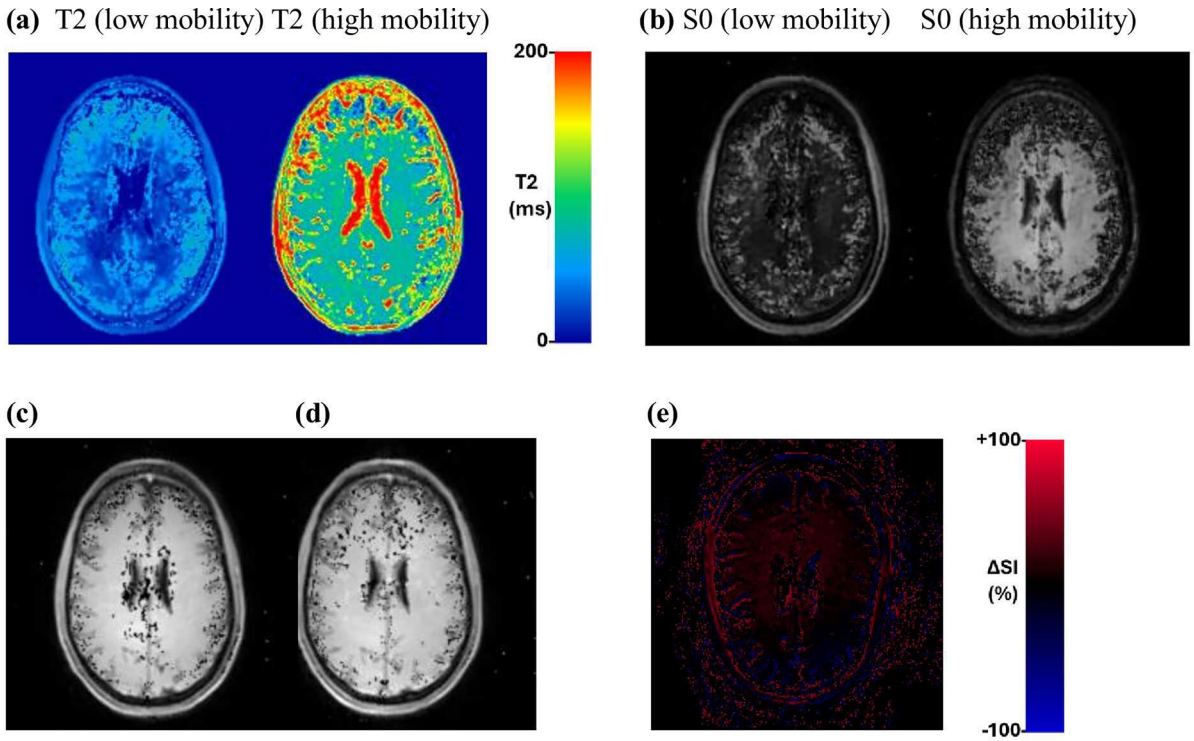

Extended Data Fig. 6 | Regional S0 images from T2 fitting of multi-echo data maps are unaltered after marathon running. To assess further the lack of post-run dehydration as a confounding factor in MWF values, we analyzed images as described below: 1) We carried out a bi-exponential decay analysis on acquired T2 multi-echo sets of images to obtain (**a**) 2 sets of T2 maps (low and high mobility protons) and (**b**) 2 sets of S0 images (Signal extrapolated at TE=0 ms). (**c**) Total S0 maps were obtained by adding the two individual S0 components. 2) CSF regions were segmented out, registering pre- (**c**) and post-run images (**d**). 3) Percentage of change of S0 images were determined pixel by pixel for each subject using the following image operation 100*(pre-post)/pre (**e**). Notice that maps reflect % changes. Subjects were scanned with identical acquisition sequence in the same scanner, with equal repetition time and flip angle. At fixed T1 weighting changes on water content should be reflected as change in S0 maps between pre- and post-run.

https://doi.org/10.1038/s42255-025-01244-7

WHITE MATTER						
Region	Pre run		Post run		Post vs Pre	t-test
	Mean	Stdev	Mean	Stdev	% change	p-value
Middle cerebellar peduncle	44.7	2.8	43.9	2.5	-1.4	0.263
Pontine crossing tract	47.0	3.6	47.0	2.4	0.4	0.480
Genu of corpus callosum	47.1	7.5	45.9	5.2	-1.5	0.249
Body of corpus callosum	47.3	6.5	47.6	6.9	2.0	0.458
Splenium of corpus callosum	44.1	4.1	44.0	5.0	0.5	0.483
Fornix (column and body of fornix	34.0	7.3	34.6	5.4	4.8	0.402
Corticospinal tract	45.7	3.0	44.9	2.3	-1.2	0.214
Medial lemniscus	45.4	2.6	45.1	2.2	-0.4	0.332
Inferior cerebellar peduncle	44.2	2.9	44.0	3.0	-0.3	0.387
Superior cerebellar peduncle	41.1	3.4	40.5	3.3	-1.2	0.230
Cerebral peduncle	47.1	3.2	45.9	3.3	-2.2	0.127
Anterior limb of internal capsule	49.6	8.8	50.1	7.4	3.0	0.410
Posterior limb of internal capsule	45.7	3.4	44.9	3.6	-1.2	0.249
Retrolenticular part of internal capsule	47.0	4.1	45.9	4.7	-1.7	0.219
Anterior corona radiata	42.8	5.1	41.9	3.2	-1.2	0.223
Superior corona radiata	43.0	2.8	42.9	3.4	0.0	0.441
Posterior corona radiata	44.2	3.5	44.4	4.4	0.9	0.407
Posterior thalamic radiation	43.7	3.7	45.3	7.3	4.0	0.152
Sagittal stratum	47.1	5.2	49.1	7.5	4.8	0.132
External capsule R	53.7	11.5	53.4	10.2	1.5	0.461
Cingulum (cingulate gyrus)	48.5	6.7	48.8	8.6	1.2	0.447
Cingulum (hippocampus)	45.2	4.1	43.0	4.6	-4.3	0.042
Fornix (cres) / Stria terminalis	47.8	3.5	47.5	5.0	-0.1	0.419
Superior longitudinal fasciculus	42.0	3.2	42.3	4.0	1.0	0.372
Superior fronto-occipital fasciculus	47.8	5.2	49.4	9.3	4.8	0.295
Inferior fronto-occipital fasciculus	54.9	12.5	50.8	9.3	-5.6	0.058
Uncinate fasciculus	50.7	8.1	47.0	8.6	-6.6	0.028
Tapetum	42.2	6.6	43.5	7.9	4.2	0.253

Extended Data Fig. 7 | Regional S0 images from bi-exponential fitting of T2 multi-echo data maps of white matter regions. Values (mean ± stdev) derived from S0 images obtained after bi-exponential fitting of T2 multi-echo data images for all subjects. White matter regions were mapped using atlas in Ref. 18. Comparisons were made using one-tail paired Student's t-test.

https://doi.org/10.1038/s42255-025-01244-7

GRAY MATTER						
Region	Pre run		Post run		Post vs Pre	t-test
	Mean	Stdev	Mean	Stdev	% change	p-value
superior_frontagyrus	27.8	1.9	26.9	4.2	-3.1	0.178
middle_frontagyrus	28.8	2.5	27.3	5.4	-4.6	0.137
inferior_frontagyrus	30.1	3.0	28.6	5.3	-4.8	0.112
precentragyrus	29.8	3.2	28.4	6.0	-5.2	0.095
middle_orbitofrontagyrus	32.6	5.5	32.0	5.1	-1.4	0.228
lateraorbitofrontagyrus	29.6	4.2	29.0	4.8	-1.6	0.259
gyrus_rectus	26.2	2.8	27.0	5.4	3.5	0.279
postcentragyrus	29.2	3.3	28.2	6.0	-4.0	0.153
superior_parietagyrus	31.9	3.0	30.8	6.2	-3.4	0.202
supramarginagyrus	27.5	3.8	26.5	5.6	-4.2	0.116
angular_gyrus	29.8	3.7	28.9	5.2	-3.3	0.140
precuneus	37.3	4.9	35.1	5.5	-5.2	0.069
superior_occipitagyrus	35.5	3.3	33.8	5.8	-4.7	0.093
middle_occipitagyrus	35.2	4.3	35.1	4.9	-0.1	0.453
inferior_occipitagyrus	38.0	6.3	39.0	6.4	3.9	0.202
cuneus	41.2	4.1	40.3	4.9	-1.6	0.259
superior_temporagyrus	32.5	4.9	32.1	5.9	-0.6	0.373
middle_temporagyrus	32.5	6.9	31.7	7.8	-1.6	0.277
inferior temporagyrus	32.5	6.1	32.5	6.3	1.6	0.484
parahippocampagyrus	38.2	3.0	37.9	5.7	-0.1	0.432
linguagyrus	41.8	3.8	42.5	5.2	2.3	0.275
fusiform gyrus	41.3	6.0	41.4	7.6	1.1	0.473
insular_cortex	46.0	7.9	43.1	7.4	-5.4	0.049
cingulate_gyrus	43.0	4.3	40.0	6.8	-6.6	0.038
caudate	46.9	9.4	46.0	8.9	-0.2	0.331
putamen	52.7	9.7	49.2	6.7	-4.9	0.053
hippocampus	40.1	3.6	39.4	8.0	-1.3	0.357
cerebellum	32.2	4.4	32.5	5.5	1.0	0.435
brainstem	38.7	3.1	38.1	3.1	-0.9	0.354

Extended Data Fig. 8 | Regional S0 images from bi-exponential fitting of T2 multi-echo data maps of gray matter regions. Values (mean ± stdev) derived from S0 images obtained after bi-exponential fitting of T2 multi-echo data images for all subjects. Gray matter regions were mapped using atlas in Ref. 19. Comparisons were made using one-tail paired Student's t-test.

https://doi.org/10.1038/s42255-025-01244-7

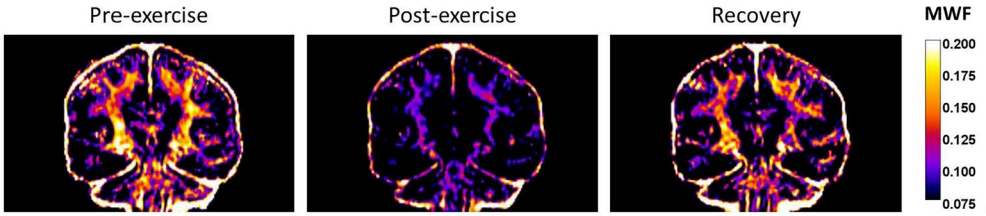

Extended Data Fig. 9 | Myelin water fraction (MWF) imaging from all subjects together showing post-run signal decay and recovery thereafter. Left, Slab volumes (average intensity projection) of MWF maps from 5 consecutive coronal slices centered in motor descending pathways from all subjects (mean MWF of scanned individuals) at imaging sessions before the marathon (pre-exercise), after (post-exercise) (n=10) and at 2-months of recovery (n=6). Color code bar displays represented values. Notice that MWF values return to pre-run values at 2-months of recovery.

https://doi.org/10.1038/s42255-025-01244-7

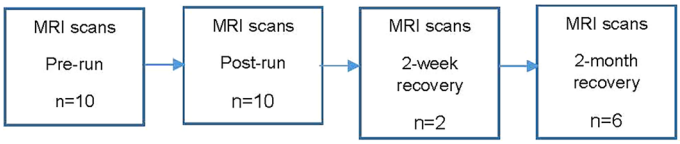

Extended Data Fig. 10 | CONSORT diagram showing number of MRI scanned subjects at all stages. Diagram illustrates the time points at which the runners were scanned. Imaging sessions were carried out 24–48 hours before (Pre-run) and after (Post-run) the marathon ($n = 10$), two weeks ($n = 2$) and two months later ($n = 6$).

nature portfolio

Corresponding author(s): Carlos Matute

Last updated by author(s): 2025/01/27

Reporting Summary

Nature Portfolio wishes to improve the reproducibility of the work that we publish. This form provides structure for consistency and transparency in reporting. For further information on Nature Portfolio policies, see our Editorial Policies and the Editorial Policy Checklist.

Statistics

For all statistical analyses, confirm that the following items are present in the figure legend, table legend, main text, or Methods section.

n/a	Confirmed	
☐	☒	The exact sample size (*n*) for each experimental group/condition, given as a discrete number and unit of measurement
☐	☒	A statement on whether measurements were taken from distinct samples or whether the same sample was measured repeatedly
☐	☒	The statistical test(s) used AND whether they are one- or two-sided *Only common tests should be described solely by name; describe more complex techniques in the Methods section.*
☐	☒	A description of all covariates tested
☐	☒	A description of any assumptions or corrections, such as tests of normality and adjustment for multiple comparisons
☐	☒	A full description of the statistical parameters including central tendency (e.g. means) or other basic estimates (e.g. regression coefficient) AND variation (e.g. standard deviation) or associated estimates of uncertainty (e.g. confidence intervals)
☐	☒	For null hypothesis testing, the test statistic (e.g. *F*, *t*, *r*) with confidence intervals, effect sizes, degrees of freedom and *P* value noted *Give P values as exact values whenever suitable.*
☒	☐	For Bayesian analysis, information on the choice of priors and Markov chain Monte Carlo settings
☒	☐	For hierarchical and complex designs, identification of the appropriate level for tests and full reporting of outcomes
☒	☐	Estimates of effect sizes (e.g. Cohen's *d*, Pearson's *r*), indicating how they were calculated

Our web collection on statistics for biologists contains articles on many of the points above.

Software and code

Policy information about availability of computer code

Data collection	Data were acquired with Philips Achieva DStream release 5.7 software
Data analysis	Data was processed with Excel (office 365); Image j v1.54g (NIH software); Fiji v1.54f (NIH software); ITK-Snap v4.0.1 (NIH software); FSL 6.0 ; and Phyton 3.12.2

For manuscripts utilizing custom algorithms or software that are central to the research but not yet described in published literature, software must be made available to editors and reviewers. We strongly encourage code deposition in a community repository (e.g. GitHub). See the Nature Portfolio guidelines for submitting code & software for further information.

Data

Policy information about availability of data

All manuscripts must include a data availability statement. This statement should provide the following information, where applicable:

- Accession codes, unique identifiers, or web links for publicly available datasets
- A description of any restrictions on data availability
- For clinical datasets or third party data, please ensure that the statement adheres to our policy

Numerical data, code and materials used in this work are available at DOI: 10.5281/zenodo.14726926. Raw DICOM Images from subjects are available in NIFTI format (anonymized) upon request (contact: Pedro Ramos-Cabrer, pramos@cicbiomagune.es)

Research involving human participants, their data, or biological material

Policy information about studies with human participants or human data. See also policy information about sex, gender (identity/presentation), and sexual orientation and race, ethnicity and racism.

Reporting on sex and gender	The study was performed on eight men and two women as reported in the methods section. This is a pilot study on few subjects.
Reporting on race, ethnicity, or other socially relevant groupings	N/A
Population characteristics	Age, gender and particularities of the subjects under study have been described in the manuscript.
Recruitment	Subjects participated voluntarily in this study, as stated in the manuscript. Participants were recruited by contacting runners clubs, trainers and physiotherapists. All volunteers were included in the study without self selection bias or other biases.
Ethics oversight	Comité de Etica de Investigación de Euskadi (CEImE)

Note that full information on the approval of the study protocol must also be provided in the manuscript.

Field-specific reporting

Please select the one below that is the best fit for your research. If you are not sure, read the appropriate sections before making your selection.

☒ Life sciences ☐ Behavioural & social sciences ☐ Ecological, evolutionary & environmental sciences

For a reference copy of the document with all sections, see nature.com/documents/nr-reporting-summary-flat.pdf

Life sciences study design

All studies must disclose on these points even when the disclosure is negative.

Sample size	This is a pilot study, no sample size was calculated a priori
Data exclusions	No data were excluded from analysis
Replication	Replication was not applicable to this study as all measurements were normailized to pre-run values
Randomization	N/A. All subjects were grouped together, no groups were compared in data analysis.
Blinding	Image processing and data analysis were done blinded to group allocation during data collection

Reporting for specific materials, systems and methods

We require information from authors about some types of materials, experimental systems and methods used in many studies. Here, indicate whether each material, system or method listed is relevant to your study. If you are not sure if a list item applies to your research, read the appropriate section before selecting a response.

Materials & experimental systems

n/a	Involved in the study
☒	☐ Antibodies
☒	☐ Eukaryotic cell lines
☒	☐ Palaeontology and archaeology
☒	☐ Animals and other organisms
☒	☐ Clinical data
☒	☐ Dual use research of concern
☒	☐ Plants

Methods

n/a	Involved in the study
☒	☐ ChIP-seq
☒	☐ Flow cytometry
☐	☒ MRI-based neuroimaging

Plants

Seed stocks	N/A
Novel plant genotypes	N/A
Authentication	N/A

Magnetic resonance imaging

Experimental design

Design type	Longitudinal MRI imaging of subjects before and after task performance
Design specifications	Longitudinal examination (repeated measurements) of the subjects
Behavioral performance measures	Behavior was not assessed in the study

Acquisition

Imaging type(s)	Multi-echo 3D gradient and spin echo sequence (GRASE); T1w anatomical image
Field strength	3 T
Sequence & imaging parameters	MRI scans were acquired on a 3T whole body MRI system (Achieva Dstream, Philips Medical System, Best, The Netherlands) using the internal quadrature body coil for transmission and a 32-channel phased array coil for reception. Each subject underwent an imaging protocol that included: 1) a multi-echo 3D gradient and spin echo sequence (Grase) for myelin water imaging, with the following parameters: TR = 2000 ms; 32 echoes with a minimum echo time of 9.3 ms and maximum of 298 ms; SENSE 2.5; flip angle 90º, band width in EPI frequency direction 2591; field of view (FOV) 230 mm2; 78 slices in transverse orientation; voxel size 1.2 x 1.2 x 1.8 mm; total scan time 7:08 min 2) a high-resolution T1w anatomical image in a sagittal orientation with the following parameters: TR=7.4 ms; TE=3.4 ms; matrix size 228 x 228; flip angle 9º; FOV 250 x 250 X180 mm; slice thickness 1.1 m; 300 slices, acquisition time 4:55 m.
Area of acquisition	whole brain

Diffusion MRI ☐ Used ☒ Not used

Preprocessing

Preprocessing software	FSL and Python
Normalization	Raw data were exported in DICOM format for off-line processing. First, data were converted into NIFTI format using dcm2niix. Anatomic brain images (skull stripped out) were obtained from T1-weighted images applying BET implementation from the FSL 6.0 distribution. Population distributions of T2 values were computed voxelwise from multitecho data using Julia implementation of DECAES software. For the analysis of interindividual and intraindividual changes in MWF maps, all MWF maps for subjects at different imaging sessions (pre-run, post-run, recovery and rest) were registered to a T2 weighted anatomical image of the brain of subject 1 (echo 8 of the echo train, with TE=74.48 ms) at session 1 using ANTS Syn registration. For image segmentation and assessment of MWF values in different regions of the brain, T1 weighted images were nonlinearly registered to the JHU DTI-based white matter atlas for white matter track segmentation and in parallel to the LPBA40 collection of the SRI24 brain atlas for segmentation of gray matter regions. Transformation matrices were later applied to the MWF maps, previously linearly registered to the corresponding T1W image.
Normalization template	JHU DTI-based white matter atlas for white matter track segmentation LPBA40 collection of the SRI24 brain atlas for Gray matter segmentation
Noise and artifact removal	No noise and artifact removal were done
Volume censoring	Anatomic brain images (skull stripped out) were obtained from T1-weighted images applying BET implementation from the FSL 6.0 distribution.

Statistical modeling & inference

Model type and settings: univariate

Effect(s) tested: student t-test

Specify type of analysis: ☐ Whole brain ☒ ROI-based ☐ Both

Anatomical location(s): automatic segmentation of brain regions using the JHU DTI-based white matter atlas for white matter track segmentationand th LPBA40 collection of the SRI24 brain atlas for Gray matter segmentation

Statistic type for inference (See Eklund et al. 2016): N/A, no fMRI data have been analyzed in this study

Correction: N/A, no fMRI data have been analyzed in this study

Models & analysis

n/a	Involved in the study
☒	☐ Functional and/or effective connectivity
☒	☐ Graph analysis
☒	☐ Multivariate modeling or predictive analysis